

Characterization of tissue microstructure using ultrasonic backscatter: Theory and technique for optimization using a Gaussian form factor

Michael L. Oelze^{a)}

*Bioacoustics Research Laboratory, Department of Electrical and Computer Engineering,
University of Illinois, 405 North Mathews, Urbana, Illinois 61801*

James F. Zachary

Bioengineering Program, University of Illinois, 1406 West Green Street, Urbana, Illinois 61801

William D. O'Brien, Jr.

*Bioacoustics Research Laboratory, Department of Electrical and Computer Engineering,
University of Illinois, 405 North Mathews, Urbana, Illinois and Bioengineering Program,
University of Illinois, 1406 West Green Street, Urbana, Illinois 61801*

(Received 13 December 2001; revised 14 June 2002; accepted 20 June 2002)

Characterization of tissue microstructure through ultrasonic backscatter is hypothesized to aid in detection and classification of diseased tissues. Radio frequency signals backscattered from tissues can be modeled according to the assumed shape, size, and distribution of scatterers in tissues. Power spectra of rf backscattered signals describe the frequency dependence of scatterers. Experimental measurements of ultrasonic backscatter from spontaneous mammary tumors in rats are obtained over the frequency range of 4 to 12 MHz. The power spectra measured from rat tumors are compared to theoretical power spectra derived from a 3D spatial autocorrelation function assuming a Gaussian distribution. Independent values of average scatterer diameter and acoustic concentration are obtained by approximating the measured power spectrum with a best-fit line. Enhanced B-mode images are made of the rat tumors and surrounding tissues with superimposed regions of interest quantified by estimated average scatterer sizes and acoustic concentrations. Scattering properties estimated inside the tumors and in surrounding tissues are shown to be distinct. Overall, estimates showed a 44.8% increase of average scatterer diameter inside the tumor as compared to tissues outside the tumor. With the exception of one rat, all estimates of the scatterers' average acoustic concentration inside the tumor were less than outside the tumors. © 2002 Acoustical Society of America. [DOI: 10.1121/1.1501278]

PACS numbers: 43.80.Qf, 43.80.Vj [FD]

I. INTRODUCTION

Conventional B-mode images of living tissues created with a clinical ultrasound scanning system are made from radio frequency (rf) envelope-detected echo signals. The rf echo signals are created by reflections from interfaces between acoustically different regions and by incoherent scattering from tissue microstructures. The rf echoes are hypothesized to contain frequency-dependent details about the smaller-scale structures (less than the wavelength) in the tissues. Generally, processing of conventional B-mode images removes the frequency-dependent information. Conventional B-mode images relate the envelope of the backscattered rf echoes to a gray scale. The conventional B-mode scanners (bandwidths of 1 to 10 MHz) can resolve structures on the order of hundreds of micrometers to centimeters in scale.¹ In order to display and quantify the smaller-scale structures of tissues, the frequency-dependent information must be utilized.

The frequency dependence of scattering from small structures (compared to wavelength) has been used to extract

details about the structures of different materials and media. As noted by Insana,² light scattering from lasers has been used to characterize the internal structure of glasses and polymers,³ and x rays have been used to characterize the structure of atoms.⁴ In acoustics, low-frequency sound waves (below 1 kHz) have been used to measure the size and distribution of turbulence in the atmosphere.⁵

In a statistical sense, the frequency dependence of ultrasound backscatter can be used to extend the resolution of conventional B-mode imaging to tens of micrometers. Ultrasonic backscattering techniques have been used to characterize different aspects of microstructure in biological tissues. Specifically, backscatter has been used to extract the average scatterer sizes and acoustic concentrations (product of the number concentration of scatterers times the relative impedance difference between the scatterers and surrounding tissues) from biological tissues. Feleppa *et al.*⁶ used frequency-dependent backscatter to quantify the scatterer sizes and acoustic concentration of ocular tumors. Lizzi *et al.*⁷ used the same techniques to examine the structure of the liver, while Insana *et al.*⁸ used these techniques to parametrize renal tissues. Numerous other experiments and detailed scattering

^{a)}Electronic mail: oelze@brl.uiuc.edu

models have been developed and used to describe backscattered ultrasound from biological tissues.⁹

Acoustic scattering theories for biological tissues assume that the tissues can be modeled as inhomogeneous fluids.² Scattering occurs when an acoustic wave propagates across a region that has a different density and/or compressibility relative to the surrounding tissue or fluid. In most cases, a sphere, a cylinder, or some simple geometric configuration has been used to approximate the scattering particle shape. If the size (diameter) of the scatterer is on the same order or smaller than the wavelength of sound, then the pattern of the scattered signal is well known for simple geometric shapes.¹⁰ In addition, the size and shape of the scattering region determine the magnitude at which a specific frequency of sound will be scattered.

For example, in tumor pathology these scattering regions as viewed by a pathologist using an optical microscope include typical macrostructures such as tumor nodules, and microstructures such as epithelial cells. Tumor nodules could range in size from millimeters to centimeters in diameter. Epithelial cells measuring 10–20 μm in diameter could be arranged as individual cells in supporting stroma. In addition, epithelial cells could also be arranged in tubules or glands that measure 50–150 μm in diameter. These epithelial cells are supported by a stroma composed of connective tissue and blood vessels that have a unique tissue density and can also encapsulate the mass and form a tumor nodule (macrostructure).

Enhanced B-mode images can be constructed by relating scattering information (estimated average scatterer size and acoustic concentration in this study) about the tissue microstructure obtained from the backscattered rf signals to selected pixels or regions of interest (ROIs). Enhanced images are formed by superimposing the quantified estimates on conventional B-mode images.¹¹ An enhanced imaging technique that could be adapted for real-time *in situ* clinical diagnosis (classification) of cancerous tissues would have enormous medical significance.

This study examines the estimation of scattering properties like the average scatterer size and acoustic concentration in order to construct enhanced B-mode images. Section II outlines the theory used to model the tissue microstructures. Section III outlines a novel estimation scheme used to invert the model from the measured data and obtain the average scatterer parameters. The new estimation scheme does not assume that the scattered power spectrum has linear frequency dependence. Instead, the new estimation scheme uses a least-squares procedure to fit a line to a measured form factor and relates the slope and intercept of that line to average scatterer properties. Section IV discusses the expected variance inherent in the estimation scheme used. Section V shows enhanced B-mode images of four rats with spontaneous mammary tumors and compares scattering properties from ROIs inside the tumors and in surrounding tissues. The final section gives some concluding remarks and future directions for this work.

II. THEORETICAL DESCRIPTION

Scattering in tissues arises from spatial changes in the acoustic impedance about the local mean value. If the wavelength of ultrasound is larger than or on the same order as the size of a scattering region, some of the incident acoustic energy will be scattered in all directions. The amount of energy scattered in any one direction will depend on the size, shape, and orientation of the scatterer relative to the wavelength and propagation direction of sound.¹² Backscatter refers to that portion of the scattered field directed back to the source aperture. The frequency content of the backscattered pulse will also depend on the size and shape of the scatterer.

The tissue model used in this study assumes a sparse collection of randomly distributed, weakly scattering particles (Born approximation). Under the assumption of weak scattering, multiple scattering is assumed to be negligible. Because the scatterers are randomly distributed, the rf backscattered signal will be due to incoherent scattering. In the specific case of the rat tumors, it is expected that there may exist distinct regions of homogeneous scattering. The homogeneous regions could lead to a coherent scattering component. If the homogeneous regions were several wavelengths in size, then the effects of coherent scatter from these regions would be outside the analysis bandwidth. The effects of the coherent scatter were assumed negligible and thus were ignored.^{8,13} The exact location and size of each scatterer cannot be determined, but rather a statistical description of average properties within a certain volume of interest may be deduced.^{13–15}

The size, shape, distribution, and elastic properties of the scatterers in the medium will determine the frequency dependence of the backscattered signals. In the tissue model, 3D spatial autocorrelation functions can be used to describe the size, shape, elastic properties, and distribution of scatterers.^{13–16} Instead of calculating the correlation functions directly for the scattering medium, some authors have found it convenient to calculate the acoustic intensity form factor F .^{14,15} The form factor is proportional to the Fourier transform of the autocorrelation function and describes the frequency dependence of the scattering in terms of the size, shape, and elastic properties of the scatterers. The Fourier transform of the autocorrelation function for statistically stationary scattering is defined as the power spectrum and incorporates the form factor. Insana *et al.* showed that in the special case of randomly positioned, spherical scatterers the form factor is a function of the average effective scatterer size (diameter) and the frequency.¹⁴

For the present study the Gaussian form factor is used to model the soft tissue scattering from spontaneous mammary tumors in rats. The Gaussian form factor has been used to model the scattering properties of many soft tissues.^{7,17,18} The choice of the Gaussian form factor over other form factors (exponential and spherical shell) was made because the average chi-square value between the measured form factor and the theoretical form factors was smallest with the Gaussian. The Gaussian form factor, as derived by Insana *et al.*, is given by¹⁴

$$F_{\text{Gauss}}(2k) = e^{-0.827k^2 a_{\text{eff}}^2}, \quad (1)$$

where k is the acoustic wave number and a_{eff} is the average effective scatterer radius. The Gaussian form factor represents a spherical scatterer that varies continuously with the surrounding tissues and has a uniform particle radius (see Ref. 9, Chap. 4, Appendix B). Instead of a sharp discontinuity with the impedance like a solid or fluid-filled sphere or spherical shell, the Gaussian scattering particle is represented by a gradual change in the impedance from the surrounding tissues. Instead of having a definite radius like the spherical shell or a solid or fluid-filled sphere, the Gaussian function has an effective radius, a_{eff} , that is related to particle shape or impedance distribution. In the tumor model (rat fibroadenoma) used in this study, tubules and glands formed by neoplastic epithelial cells ranged between 50–150 μm in diameter. These structures were distributed at random in a supporting matrix composed principally of well-collagenized fibrous connective tissue.

Typical backscatter measurements from tissue volumes are made by choosing a region of interest (ROI) and gating the backscattered rf time signal corresponding to the ROI. The measured power spectrum is the magnitude squared of the Fourier transform of the gated, rf time signal. The effects of the gating function (windowing function) and beam function of the transducer (weakly focused piston transducer near the focal plane) are needed to properly model the backscattering measurement. Lizzi *et al.* incorporated the gating function (Hanning window) and beam pattern effects in the development of the model to normalize the theoretical backscattered power spectrum.¹⁶ In the frequency domain, the normalized, theoretical power spectrum is given by

$$W(f) = \frac{185Lq^2a_{\text{eff}}^6\rho z_{\text{var}}^2f^4}{[1 + 2.66(fqa_{\text{eff}})^2]} e^{-12.159f^2a_{\text{eff}}^2}, \quad (2)$$

with L the gate length (mm), q the ratio of aperture radius to distance from the region of interest, and f is the frequency (MHz). The quantity, ρz_{var}^2 , is termed the acoustic concentration and is the product of the number of scattering particles per unit volume (mm^{-3}), ρ , and the fractional change in the impedance between the scattering particles and the surrounding medium, $z_{\text{var}} = (Z - Z_0)/Z_0$, where Z is the acoustic impedance of the scatterers and Z_0 is the acoustic impedance of the surrounding medium. The exponential term is the Gaussian form factor term in the frequency domain.

The measured power spectrum is the magnitude squared of the Fourier transform of the gated time signal. The effects of the equipment on the power spectrum measurement are factored out by dividing by a calibration spectrum.^{13,15} To obtain the calibration (reference) spectrum, a pulse is reflected from a planar surface with known reflectivity and received by the emitting transducer. The transducer is a single element, piston style, and weakly focused. The same transducer, equipment, and settings are used to send and receive the reflected pulses that are used to obtain the backscattered signals from a selected ROI in the tissue. The planar surface is located at the same axial distance from the transducer as the center of the ROI selected in the tissue (in the focal zone of the transducer). The measured power spectrum of the signal from the gated ROI in the tissue is divided by the power spectrum of the reference signal.

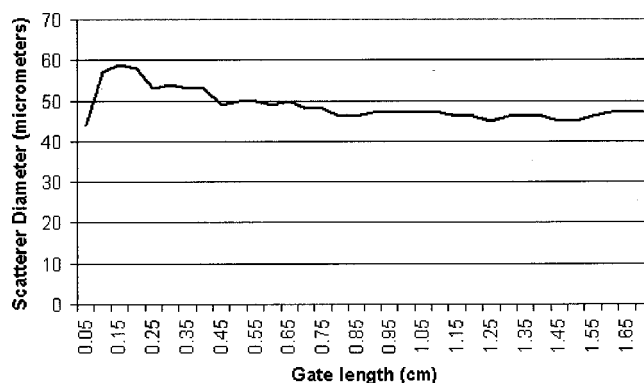


FIG. 1. Estimated scatterer diameters from Gaussian-type particles in a simulated random scattering medium versus gated length of the backscattered rf signal.

The data must be acquired from a large enough volume in order to obtain good estimates because the measured power spectrum describes statistical properties of the medium. Several authors have examined the relationship between the size of the ROI (gate length) and the estimation of scattering power and scatterer statistics.^{16,19–22} As the size of ROI is increased, the statistical estimations should converge for a random scattering medium. Two important factors are key to choosing an appropriate gate length. First, the time–bandwidth product should be greater than 1. Second, a larger gate length means that more scatterers will be included in the spectrum. The sum of the random phase contributions from a large amount of scatterers is more likely to cancel than from a few randomly spaced scatterers. Topp *et al.*¹⁹ examined the question of convergence and concluded that adequate estimations could be obtained by taking ROIs with gate lengths of 10 or more wavelengths at the center frequency of interrogation. Figure 1 shows estimations of scatterer diameter made from a computer software phantom. The scatterer size estimates were made using the estimation scheme outlined in Sec. III. The particles in the software phantom scattered according to the Gaussian form factor with an effective diameter of 49 μm . The impedance of the scattering particle, Z , was given the value of glass (density 2.38 g/cm^3 , longitudinal sound speed 5570 m/s) and the impedance of the surrounding medium, Z_0 , was given the value for agar (density 1.0 g/cm^3 , longitudinal sound speed 1540 m/s). The center frequency of the incident pulse and analysis bandwidth was around 7 MHz ($\lambda = 0.22$ mm) with a 70% bandwidth defined at -6 dB (half-power bandwidth of the pulse–echo signal). The scattering was assumed to occur in the focal zone of a transducer with an f-number of 5, where the value of q would be very small. From Fig. 1 it is seen that the estimations of scatterer diameter begin to converge to 49 μm at a gate length of about 2.5 mm, or 11 wavelengths of the center frequency.

Typically, a ROI is made up of a number of parallel gated A lines of the same length. The power spectrum measured from an individual A line may have sharp fluctuations (noise) due to the random nature of the scatterer spacings in the medium.²³ The fluctuations represent deviations from the shape of the power spectrum modeled with the form factor. Consecutive parallel A lines should have similar statistical

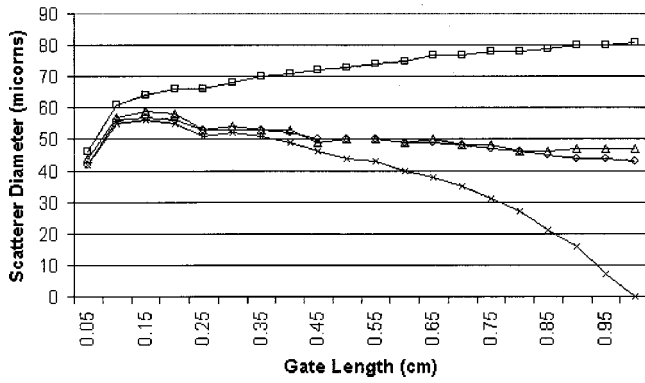


FIG. 2. Estimated scatterer diameters from Gaussian-type particles in a simulated attenuating medium (8 dB/cm @7 MHz) using attenuation compensation and no attenuation compensation; Δ , unattenuated signal; \square , uncompensated attenuated signal; \times , point compensated attenuated signal; \diamond , compensated signal using Eq. (6).

properties if located near each other. The difference between rf echoes from the consecutive A lines will be the difference in random spacings of the scatterers. If the statistical properties of consecutive A lines can be assumed the same, then averaging the consecutive A lines should reduce the random fluctuations seen in a single A-line spectrum. Averaging will yield a better overall description of the scatterer statistical properties. The average measured power spectrum is given by

$$W_{\text{meas}}(f) = \frac{1}{N} \frac{\Re^2}{4} \sum_{n=1}^N \frac{|FT\{p_n(t)\}|^2}{W_{\text{ref}}(f)}, \quad (3)$$

where \Re is the reflection coefficient of the planar reflector, $p_n(f)$ is the gated rf time signal of the n th A line, N is the number of gated A lines, and $W_{\text{ref}}(f)$ is the reference power spectrum.

The measured power spectrum describes the frequency dependence of the scatterers in the medium. Frequency-dependent attenuation will affect the measured power spectrum and, if not compensated for, give rise to inaccurate estimates of scattering properties. Typically, attenuation increases with frequency. The slope of the power spectrum will be more negative if the frequency-dependent losses are not taken into account. In order to give optimal estimations of scattering properties, the frequency-dependent attenuation must be compensated. If the gate size were infinitesimally small, the frequency-dependent attenuation losses could be compensated, assuming constant attenuation, by simple-point attenuation compensation given by¹⁴

$$W_{\text{comp}}(f) = W_{\text{meas}}(f) e^{4\alpha(f)x}, \quad (4)$$

where $\alpha(f)$ is the frequency-dependent attenuation and x is the propagation distance through the attenuating medium to the center of the gated region. When the gate length is not small and the attenuation is not negligible, point compensation does not correctly account for frequency-dependent losses. Figure 2 shows estimations of scatterer sizes from software phantoms with large attenuation (8 dB/cm @7 MHz) as the gate length is increased using the point-attenuation-compensation function and no attenuation compensation. The large attenuation was used to coincide with

the attenuation measured in rat intercostal tissues (1.1 dB/cm/MHz).²⁴ Point-attenuation compensation causes an underestimation of the average scatterer diameter, while not accounting for frequency-dependent attenuation leads to an overestimation of scatterer diameter. Attenuation-compensation functions exist that account for frequency-dependent losses to the measured power spectrum obtained from gates of finite length.^{25–27} The attenuation-compensation functions are represented by

$$W_{\text{comp}}(f) = W_{\text{meas}}(f) A(f, L), \quad (5)$$

where L is gate length. An attenuation-compensation function derived for gated signals was used in this study, and is given by²⁷

$$A(f, L) = e^{4\alpha_0(f)x_0} \left[\frac{2\alpha(f)L}{1 - e^{-2\alpha(f)L}} \right]^2, \quad (6)$$

where $\alpha_0(f)$ and x_0 are, respectively, the attenuation and propagation distance of the intervening tissues and $\alpha(f)$ is the attenuation coefficient in the gated region (assumed constant).

III. MODEL INVERSION

Several techniques have been used to parametrize the shape of the measured power spectrum or to estimate properties of the scatterers in a tissue from the shape of the measured power spectrum. These techniques relate the theoretical models to the measured backscatter data. Enhanced images are then formed with the spectral parameters or the estimated scatterer properties in order to aid in identifying and characterizing diseased tissues. Several authors have successfully used enhanced (parametric) images of the backscatter coefficient and attenuation to aid in tissue characterization.^{15,16,19,28–31} Zagzebski *et al.* used the backscatter coefficient parametric images to classify diseased liver.²⁹ Other researchers have used the slope and intercept of the measured backscattered power spectrum to create parametric images.¹⁹ Feleppa *et al.*³⁰ and Lizzi *et al.*¹⁶ have used the intercept, slope, and midband fit to the measured backscattered power spectrum and create parametric images that aided in detection and classification of cancer in the eye and prostate. Insana and Hall¹⁵ created parametric images from scatterer size estimates, scattering strength measurements, chi-square images, and integrated backscatter coefficient images. The chi-square images were important to show how well the model represented the interrogated medium for any particular ROI.

If the deduced parameters are related to actual physical properties of the tissues, i.e., the average scatterer size and acoustic concentration, it may be possible to partially verify the particular form factor models through other means. Possible verification of the model might also be obtained through light microscopy. Ultrasound waves detect changes in the mechanical (compressibility, density) properties of the tissues, while light microscopy detects electromagnetic (dielectric) changes in the tissues. Scattering particles are expected to have both mechanical and electromagnetic differences with surrounding tissues. There will not be a one-to-

one correlation between mechanical and electromagnetic property changes in the scattering particles, but the optical characteristics should give an approximation of shape and size that can be related to acoustic estimations and aid in verification of the form factor models. Estimation of the size and acoustic concentration properties of scatterers is desirable because they are hypothesized to relate directly to morphological features in the tissues examined.

Insana and Hall¹⁵ estimated the average scatterer size by minimizing the average squared difference (MASD) between the theory and measurements over a range of scatterer size values. The MASD between the theoretical normalized power spectrum and the measured power spectrum is calculated by¹⁴

$$\text{MASD} = \min \left(\frac{1}{m} \sum_{i=1}^m (X_i - \bar{X})^2 \right), \quad (7)$$

with

$$X_i = 10 \log [W_{\text{meas}}(f_i) A(f_i, L) F_{\text{Gauss}}(a_{\text{eff}}, f_i) / f_i^4], \quad (8)$$

and

$$\bar{X} = \frac{1}{m} \sum_{i=1}^m X_i, \quad (9)$$

where A is the attenuation-compensation term and m is the number of points in the frequency data bandwidth. The estimate of the average scatterer diameter is the argument that minimizes Eq. (7).

Typically, the measured power spectrum is in terms of the scatter strength, a decibel scale

$$S_{\text{meas}}(f) = 10 \log [W_{\text{comp}}(f)]. \quad (10)$$

Inverting the measurement of the backscattered power spectrum with the theoretical spectrum enables scattering parameters to be estimated. Relating Eq. (10) to Eq. (2) gives

$$S_{\text{meas}}(f) = 10 \log \left\{ \frac{185 L q^2 a_{\text{eff}}^6 \rho z_{\text{var}}^2 f^4}{[1 + 2.66(f q a_{\text{eff}})^2]} e^{-12.159 f^2 a_{\text{eff}}^2} \right\}. \quad (11)$$

Expanding the logarithm in Eq. (11) yields

$$\begin{aligned} S_{\text{meas}}(f) &= 10 \log [185 L q^2 a_{\text{eff}}^6 \rho z_{\text{var}}^2] \\ &\quad - 10 \log [1 + 2.66(f q a_{\text{eff}})^2] \\ &\quad - 10(12.159 f^2 a_{\text{eff}}^2) \log e + 10 \log f^4. \end{aligned} \quad (12)$$

Typically, the ratio of transducer radius to distance from transducer to ROI is small ($q \ll 1$), which allows the second term on the right-hand side to be approximated by

$$\log(1+x) \approx x \log e \quad (\text{for small } x), \quad (13)$$

because the value $2.66(f q a_{\text{eff}})^2 \ll 1$. Subtracting the f^4 term from the right-hand side gives

$$S_{\text{meas}}(f) - 10 \log f^4 \approx M(a_{\text{eff}}^2) f^2 + I(a_{\text{eff}}^6, \rho z_{\text{var}}^2), \quad (14)$$

where

$$M(a_{\text{eff}}^2) = -4.34[12.159 + 2.66 q^2] a_{\text{eff}}^2, \quad (15)$$

and

$$I(a_{\text{eff}}^6, \rho z_{\text{var}}^2) = 10 \log [185 L q^2 a_{\text{eff}}^6 \rho z_{\text{var}}^2]. \quad (16)$$

Comparing Eq. (14) to that of a line ($y = mx + b$), where $x = f^2$, it is seen that the intercept, I , is a function of the effective average radius (diameter) of the scatterers and the acoustic concentration of scatterers. The slope, M , is a function of the average effective diameter of scatterers only. The slope and intercept of the line can be found by using least squares to fit a line to the measured data (left side) of Eq. (14). From the slope value, the average scatterer diameter is estimated. Once the average effective scatterer diameter is estimated, the average acoustic concentration of scatterers can be estimated from the intercept value and the estimated value of the scatterer diameter. The best-fit line parameters derived in Eqs. (15) and (16) differ from the linear parameters used in the estimation scheme by Lizzi *et al.* in that Eqs. (15) and (16) represent the best-fit line to the measured form factor (with some constants related to the gating and beam functions).³² The linear parameters estimated from the approach by Lizzi *et al.* are deduced from the scattered power spectrum, which is not linear over a large range of frequencies.³²

The estimation scheme described here has a distinct advantage over the MASD estimation scheme in the number of calculations needed to derive the estimates. In the MASD estimation scheme, different values for the average scatterer diameter are chosen until a minimum average squared difference is found. The summation of the squared difference values is done every time a different average scatterer diameter is tried. Several choices of scatterer diameter may be tried before the average squared difference is minimized. For each scatterer diameter tried, the squared difference must be calculated at each data point in the analysis bandwidth. In the best-fit line estimation scheme the summation of the bandwidth values is done only once and the estimated average scatterer diameter is obtained.

IV. EXPECTED VARIANCE OF ESTIMATION SCHEME

The expected variance of the estimation scheme developed in this work was calculated in order to optimize the measurement for inverting the scatterer parameters. From Chaturvedi and Insana,³³ the expected variance of the average scatterer diameter from measurement of the Gaussian form factor is given by

$$\text{var } \hat{D} \approx \sum_{j=1}^N \left\{ \text{var } \hat{F}_{\text{Gauss}}(f_j) \left(\frac{\partial D}{\partial \hat{F}_{\text{Gauss}}(f_j)} \right)^2 \right\}, \quad (17)$$

where \hat{D} is the estimated average scatterer diameter and N is the number of data points used in the analysis bandwidth. To evaluate the variance of \hat{D} , the relationship between the average scatterer diameter D and the measured form factor must be determined. Using the best-fit line technique, for small q , Eq. (14) can be rewritten as

$$S_{\text{meas}}(f) - 10 \log f^4 \approx 10 \log [\hat{F}_{\text{Gauss}}(f, D) \cdot C(D, \rho z_{\text{var}}^2)], \quad (18)$$

so that

$$10 \log[\hat{F}_{\text{Gauss}}(f, D) \cdot C(D, \rho z_{\text{var}}^2)] = M(D)f^2 + I(D, \rho z_{\text{var}}^2). \quad (19)$$

The slope M can be determined using regression to find the best-fit slope

$$M(D) = \frac{N \sum_{j=1}^N f_j^2 10 \log[\hat{F}(f_j) \cdot C] - \sum_{j=1}^N f_j^2 \sum_{j=1}^N 10 \log[\hat{F}(f_j) \cdot C]}{N \sum_{j=1}^N f_j^4 - (\sum_{j=1}^N f_j^2)^2}, \quad (20)$$

where \hat{F} represents the estimated form factor. From Eq. (15), when $q \ll 1$

$$M(D) \approx -13.2D^2, \quad (21)$$

which gives, after simplification

$$-13.2D^2$$

$$= \frac{N \sum_{j=1}^N f_j^2 10 \log \hat{F}(f_j) - \sum_{j=1}^N f_j^2 \sum_{j=1}^N 10 \log \hat{F}(f_j)}{N \sum_{j=1}^N f_j^4 - (\sum_{j=1}^N f_j^2)^2}, \quad (22)$$

where the factors involving $10 \log C$ subtract out. Defining

$$\sigma_{f^2} = N^2 \sum_{j=1}^N f_j^4 - N \left(\sum_{j=1}^N f_j^2 \right)^2, \quad (23)$$

and rearranging yields

$$\sum_{j=1}^N \left[\frac{13.2D^2}{N^2} + \frac{(f_j^2 - \bar{f}^2) 10 \log \hat{F}(f_j)}{\sigma_{f^2}} \right] = 0, \quad (24)$$

which is of the form $\sum_{j=1}^N Y_j = 0$. The chain rule of differentiation is used

$$\frac{\partial Y_j}{\partial \hat{F}(f_j)} = \frac{\partial Y_j}{\partial D} \frac{\partial D}{\partial \hat{F}(f_j)}, \quad (25)$$

with

$$\frac{\partial Y_j}{\partial D} = \sum_{j=1}^N \frac{26.4D}{N^2} = \frac{26.4D}{N}, \quad (26)$$

and

$$\frac{\partial Y_j}{\partial \hat{F}(f_j)} = \frac{4.34(f_j^2 - \bar{f}^2)}{\sigma_{f^2} \hat{F}(f_j)}. \quad (27)$$

Combining Eqs. (26) and (27) with Eq. (25) yields

$$\frac{\partial D}{\partial \hat{F}(f_j)} = \frac{4.34N}{26.4D} \frac{(f_j^2 - \bar{f}^2)}{\sigma_{f^2} \hat{F}(f_j)}. \quad (28)$$

Substituting Eq. (28) into Eq. (17) gives

$$\text{var } \hat{D} = \sum_{j=1}^N \text{var } \hat{F}(f_j) \left(\frac{4.34N}{26.4D} \frac{(f_j^2 - \bar{f}^2)}{\sigma_{f^2} \hat{F}(f_j)} \right)^2. \quad (29)$$

From Chaturvedi and Insana³³

$$\text{var } \hat{F}(f_j) \approx [F_{\text{Gauss}}(f_j)]^2 g(f_j), \quad (30)$$

with

$$g(f) = \left[1 + \left(\frac{\sin(2\pi f N_p \Delta t)}{N_p \sin(2\pi f \Delta t)} \right)^2 \right], \quad (31)$$

where Δt is the sampling interval of the time signal and N_p is the number of points in the time signal. Approximating \hat{F} by F_{Gauss} yields the result

$$\text{var } \hat{D} = \frac{2.09 \times 10^{-2} N^2}{D^2 \sigma_{f^2}^2} \sum_{j=1}^N g(f_j) (f_j^2 - \bar{f}^2)^2. \quad (32)$$

For a long time signal, $g(f_j) \approx 1$, which gives

$$\text{var } \hat{D} = \frac{2.09 \times 10^{-2}}{D^2} \left[\sum_{j=1}^N f_j^4 - N \bar{f}^2 \right]^{-1}. \quad (33)$$

Calculation of the variance of the average diameter estimation for the MASD technique gives the same value as the best-fit line estimation technique. Simulations and experiments by Chaturvedi and Insana showed that the expected variance derived for the MASD estimation scheme was valid for a Gaussian form factor.³³ The reason that the expected variance of the estimated scatterer diameter is the same for the best-fit line estimation scheme and the MASD scheme is that both techniques minimize the squared difference. The MASD finds the value of the scatterer diameter that minimizes the squared difference between the measured data and the theoretical. The best-fit line is a least-squares fit of the theoretical spectrum to the experimental spectrum. Instead of trying different values for the average scatterer diameter until the average squared difference is minimized, the best-fit line automatically minimizes the average squared difference and consequently yields the best estimate of the average scatterer diameter.

For the estimation scheme, the variance is inversely proportional to the average scatterer diameter squared. The larger the average scatterer diameter the more precise the scatterer estimation should be. However, as the relative size of the wavelength becomes smaller, the theory may not correctly describe the scattering. Likewise, estimating the scatterer parameters at higher center frequencies over a larger bandwidth also decreases the expected variance in the measurement of D . The analysis bandwidth needs to be chosen with consideration of the expected scatterer properties. Insana and Hall¹⁵ discussed the importance of keeping the ka_{eff} value within the range of 0.5 and 1.2. Using frequencies too far below the range (larger wavelength compared to scatterer size) means the signal scattered from the microstructures may be too small to be discerned from the noise. Using frequencies too far above the range (smaller wavelength compared to the scatterer size) means that the size and shape of the scatterer no longer dictates the frequency dependence. If

a certain average size of the scatterer is expected, the analysis frequency bandwidth needs to be chosen accordingly. The calculation of the expected variance in the estimation technique exhibits the trade-off between larger bandwidth and center operating frequency and the restrictions on the ka_{eff} value. The calculation of the expected variance is important to optimizing the measurement technique. The measurement technique is optimized for the variance by choosing the largest bandwidth and largest center frequency that fit within the acceptable ka_{eff} range. The dependence of the expected variance directly on $g(f)$ also shows that a better estimation may be made from a longer gated signal.

V. ENHANCED IMAGES OF RAT MAMMARY TUMORS

The least-squares best-fit line estimation scheme utilizing the Gaussian form factor model was applied to B-mode image rf data obtained from mammary tumors that had developed spontaneously in rats. The average scatterer size and acoustic concentration (physical concentration of scatterers times the average relative impedance difference between scatterers and surrounding tissues) were estimated from the rf signals used to construct the B-mode images. The experimental protocol was approved by the Laboratory Animal Care Advisory Committee at the University of Illinois at Urbana-Champaign and satisfied all campus and NIH rules for the humane use of laboratory animals. Four Sprague-Dawley rats (Harlan, Indianapolis) that had developed spontaneous mammary tumors were evaluated. Each rat was euthanized with CO_2 , and the tumor and surrounding area were immediately shaved and depilated. The rat was then placed on a holder in a tank of degassed water at 37°C for scanning with an ultrasonic transducer. A single-element broadband transducer was used to scan laterally across the tumors and surrounding tissues. The transducer was moved laterally by a micropositioning system with step size of $100\ \mu\text{m}$ between each scan. The transducer had a center frequency of about 8 MHz with an 80%–90% frequency bandwidth (Gaussian spectrum defined at $-6\ \text{dB}$). The transducer had a diameter of 12 mm and a focal length of 50 mm. Measurements were taken within or near the focal zone. The frequency and bandwidth were chosen based on the expected values of the average scatterer sizes in the rat tissues. The frequency and bandwidth were chosen so that the variance in the measurement would be minimized while keeping within the optimal ka_{eff} range. The transducer was operated in pulse/echo mode through a Panametrics 5800 pulser/receiver (Waltham, MA). The signals were recorded and digitized on an oscilloscope (Lecroy 9354 TM; Chestnut Ridge, NY) and downloaded to a PC for postprocessing. The sampling rate of the received signals was 50 MHz. Figure 3 shows a picture of the rat in a holder ready to be scanned. The mammary tumor is located on the upper left portion of the chest. The black line across the tumor and chest represents the direction and the length of the lateral scan.

Two-dimensional B-mode images were constructed from the ultrasonic scan lines from each rat. Each scan line was taken from a gated portion of the rf backscattered signal and recorded for postprocessing. The axial distance of the B-mode images was associated with the time base of the

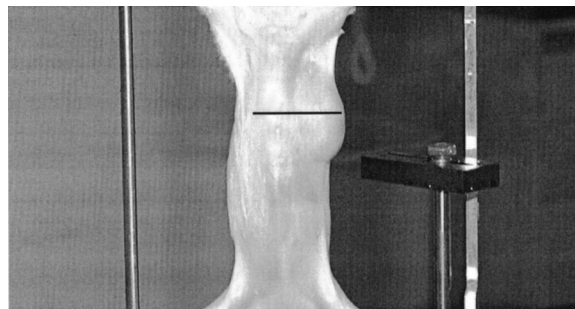


FIG. 3. Rat to be scanned in holder in tank of degassed water. Ultrasonic scans ran laterally across the chest and tumor following along the black line. The tumor is located on the upper left side of the chest.

signals, and the lateral position of the images was associated with the lateral step length where the individual scan lines were recorded. From the 2D B-mode images, ROIs were divided into regions inside and outside the tumor where the B-mode images appeared to be homogeneous (no interfaces or large echoes). The regions scanned and analyzed outside the tumors were intercostal tissues. The ROIs were separated to determine if normal surrounding tissues could be differentiated from the tissues inside the tumors based on the scatterer properties.

After scanning, the tumors were excised, fixed in 10% neutral-buffered formalin, processed, and stained with hematoxylin and eosin stain for routine histologic evaluation by light microscopy. The tumors were diagnosed as fibroadenomas following histopathologic evaluation. Figure 4 shows a photomicrograph of a tissue slice through a tumor using light microscopy. The tumor consisted of well-differentiated mammary epithelial cells arranged in tubules and glands that were distributed at random in a supporting matrix composed principally of well-collagenized fibrous connective tissue. Tubules and glands formed by neoplastic epithelial cells ranged in size between $50\text{--}150\ \mu\text{m}$ in diameter.

Scatterer estimates were made for each ROI using the best-fit line estimation scheme. The backscattered rf signal

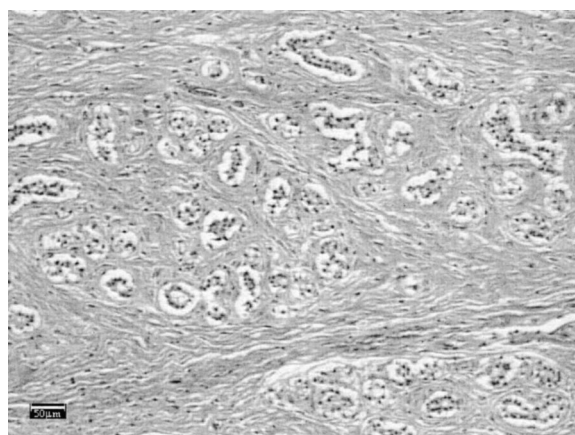


FIG. 4. Photomicrograph of a rat mammary tumor. The specimen was fixed in 10% neutral buffered formalin, dehydrated, embedded in paraffin, mounted on a glass slide, and stained with hematoxylin and eosin stain for microscopic evaluation. The tumor consists of well-differentiated epithelial cells arranged in acini surrounded by bands of fibrous connective tissue. The scale bar represents $50\ \mu\text{m}$.

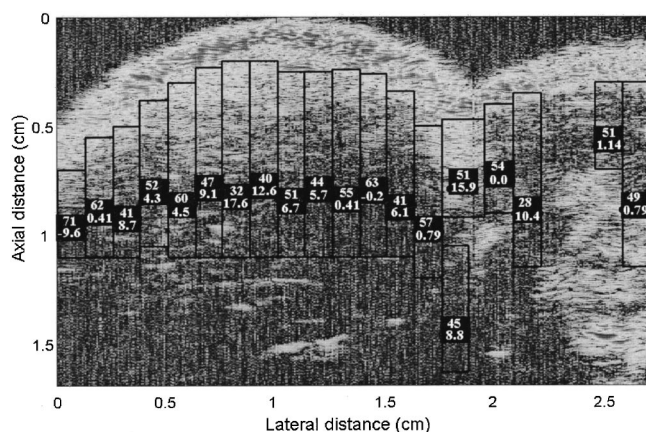


FIG. 5. Enhanced B-mode image of rat 1 with the tumor located between the lateral distance of 0 to 1.8 cm. The top number in the boxes represents the average scatterer diameter (μm) and the bottom number represents the average acoustic concentration ($10^* \log[\text{mm}^{-3}]$).

was gated from each ROI using a Hanning window and the measured power spectrum was calculated according to Eq. (3). The average scatterer diameter and average acoustic concentration were estimated from the measured power spectrum. The attenuation for the tissues was deduced from the backscatter according to the method listed in Shung and Thieme (p. 247).⁹ Regions where the scattering appeared homogeneous with depth were selected in order to estimate the best attenuation value by examining the overall loss of the backscattered signal with depth. If the region selected is homogeneous with scattering, then the only difference between scattering from particles near and farther away is the attenuation loss over the extra propagation distance. The attenuation deduced from the backscatter in a particular rat was then used to estimate the scatterer properties throughout the particular rat. The average attenuation coefficient estimated from the backscatter was 0.9 dB/cm/MHz, assuming a linear dependence.

Conventional B-mode images were constructed of the tumors and surrounding tissues. Following the enhanced imaging model of Topp *et al.*¹⁹ the average scatterer properties were superimposed in boxes corresponding to the gated ROIs. In the enhanced B-mode images by Topp *et al.*, the number inside the superimposed box represented the slope of the measured average backscatter coefficient. In this work, two numbers representing the average scatterer diameter and average acoustic concentration are listed in the ROI boxes. Figures 5–8 show enhanced B-mode images of the rat tumors and surrounding tissues. The top number represents the average scatterer diameter (micrometers) in the ROI, and the bottom number represents the average acoustic concentration (mm^{-3}). Noise is evident in the B-mode images of the rat mammary tumors. The noise is due to the low-power system used for imaging and not because of the large bandwidth.

The average scatterer properties estimated inside the tumor and outside the tumor from healthy tissues were then compared. Figure 9 shows the mean of the average scatterer diameters measured inside the tumors and outside the tumors of the four rats. An examination of the average estimated scatterer diameters inside and outside the tumors showed that

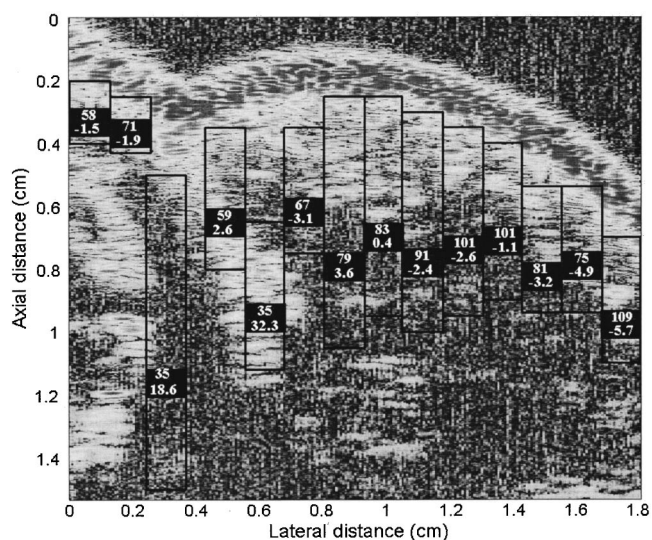


FIG. 6. Enhanced B-mode image of rat 2 with the tumor located between the lateral distance of 0.4 to 1.8 cm. The top number in the boxes represents the average scatterer diameter (μm) and the bottom number represents the average acoustic concentration ($10^* \log[\text{mm}^{-3}]$).

the scatterers inside the tumors were larger than scatterers in the surrounding normal tissues. Overall, the estimates showed a 44.8% increase of average scatterer diameter inside the tumor as compared to the tissues outside the tumor. With the exception of the first rat, all differences of scatterer size in the tumors were outside the standard deviation of scatterer size estimates outside the tumors.

Figure 10 shows the estimated average acoustic concentration inside and outside the tumors of the four different rats. With the exception of the first rat, all estimates of average acoustic concentration inside the tumor were less than the average acoustic concentration outside the tumors. Error bars representing the standard deviation are not included be-

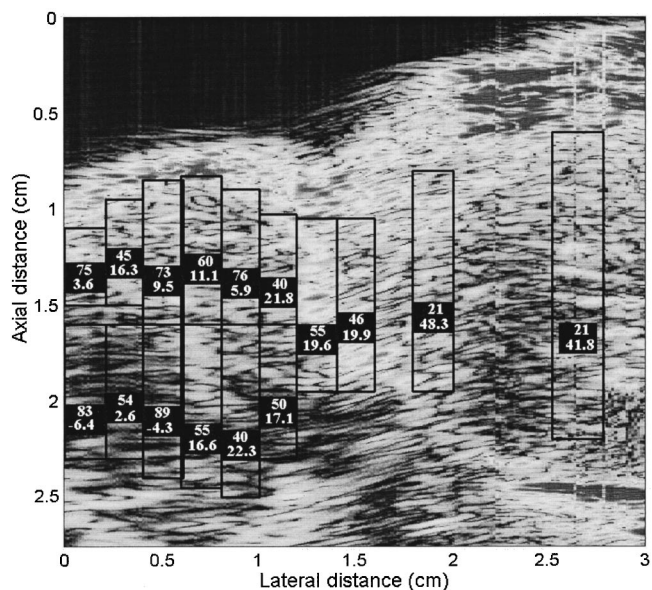


FIG. 7. Enhanced B-mode image of rat 3 with the tumor located between the lateral distance of 0 to 1.1 cm. The top number in the boxes represents the average scatterer diameter (μm) and the bottom number represents the average acoustic concentration ($10^* \log[\text{mm}^{-3}]$).

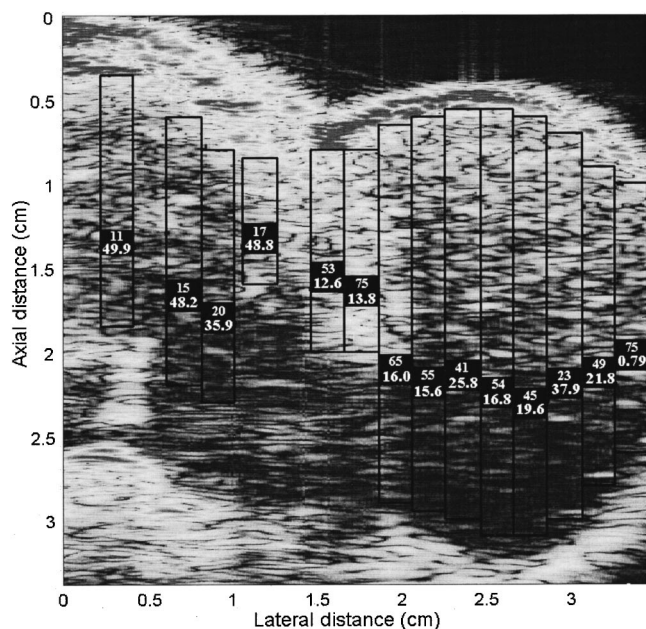


FIG. 8. Enhanced B-mode image of rat 4 with the tumor located between the lateral distance of 1.6 to 3.5 cm. The top number in the boxes represents the average scatterer diameter (μm) and the bottom number represents the average acoustic concentration ($10 \cdot \log[\text{mm}^{-3}]$).

cause, in most of the examined cases, the error bars were actually larger than the magnitude of the acoustic concentration. The large standard deviation means that the average acoustic concentration might not be a precise estimation. An estimate of the average acoustic concentration was made from the estimated intercept of the best-fit line and the estimated average scatterer radius to the sixth power. Errors in the estimate of the average scatterer radius lead to much larger errors in the average acoustic concentration. In the case where there is definite separation (no overlap between the error bars) between the average scatterer sizes (rats 2–4), a definite difference was seen between the estimated average acoustic concentration inside and outside the tumor. Where the estimated average scatterer diameters inside the tumors and outside the tumors were close (rat 1), the difference between the average acoustic concentration is very small and not a good indicator of tissue structure difference.

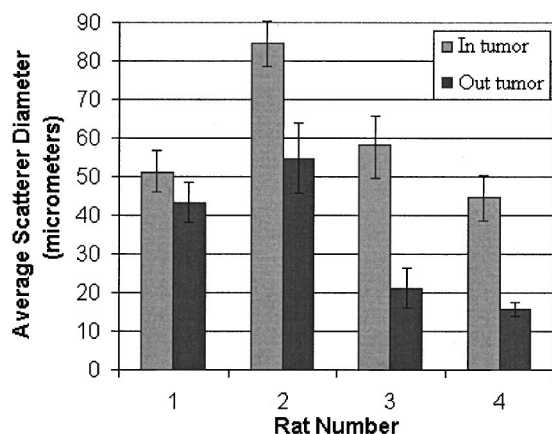


FIG. 9. Mean value of average scatterer diameters inside and outside the tumors. Error bars represent one full standard deviation about the mean.

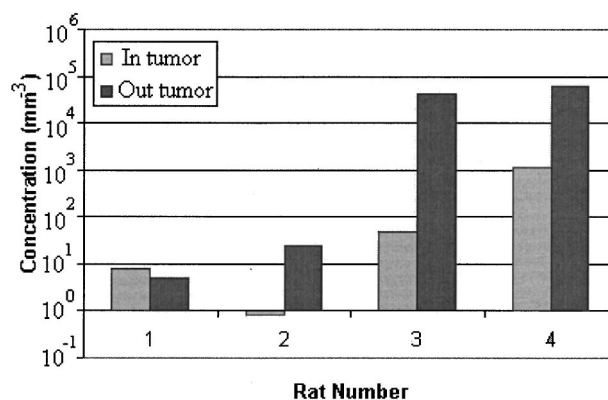


FIG. 10. Mean value of the average acoustic concentration inside and outside the tumors.

In order to verify the theory and acoustic estimates from the tumors, a comparison with the tissue microstructure through other means is necessary. Comparing the light microscopic image of Fig. 4 with the acoustic estimates of average scatterer size shows that there are structures on the same order in size. However, relating the light microscopy images with acoustic estimates may not be a valid comparison. The acoustical technique measures mechanical property changes in the tissue structure, while the light microscopy measures electromagnetic properties of the tissues. There may not be a one-to-one correlation between changes in the two properties. Much work needs to be done to verify the acoustical theory and estimation scheme by relating the estimates to actual tissue structures.

VI. CONCLUSION

An estimation scheme was devised to rapidly assess the average scatterer diameter and average acoustic concentration from soft tissues using the Gaussian form factor model. The estimation scheme works by using least squares to fit a line to the measured form factor. The precision of the estimation scheme was shown to be equivalent to the MASD scheme used by Insana *et al.*^{11,12} to obtain scatterer size estimates. The best-fit line estimation scheme takes advantage of the unique functional form of the Gaussian form factor to reduce calculation time and give rapid estimates. Previous estimation schemes assumed that the power spectrum is linear with frequency.¹⁶ The best-fit line estimation scheme assumes linear dependence for the measured form factor and not the power spectrum.

Four rats that had developed spontaneous mammary tumors were obtained and scanned with an ultrasonic transducer. The tumors and surrounding healthy tissues were interrogated in order to compare the average scatterer properties. The rf backscattered signals were gated from ROIs that were selected in each of the rats. Enhanced B-mode images were constructed from conventional B-mode images superimposed with estimated scattering parameters. The enhanced images were used to visually detect differences in tissue microstructure properties.

Comparisons of average scatterer diameters estimated inside the tumors and in the surrounding normal tissues showed that distinctions existed between the average scat-

terer properties. The distinctions could be used to classify tissues according to their microstructure. The distinctions could further be used to aid in the noninvasive diagnosis of disease.

Future work needs to be done to better account for the frequency-dependent losses produced by attenuation. The assumption that attenuation is homogeneous throughout the rat is not necessarily true. In most cases, it is expected that the attenuation and scattering properties will deviate from one region to the next. If the deviations are substantial, then a more detailed mapping of the attenuation throughout different regions will be needed to correctly account for the frequency-dependent losses to the measured power spectrum.

This study has shown that scattering properties like the average scatterer diameter and average acoustic concentration can readily be estimated from rf backscattered signals. Meaningful analysis of the statistical properties between scatterer parameters inside and outside the tumors is limited by the spontaneous nature of the tumors. The tumors grew at different places on each rat in an uncontrolled fashion. In each comparison, different surrounding tissues were compared with the tumor tissues. Future work will be done in implanting solid tumor cell lines in rats and closely managing their growth. In creating a managed line of tumors in rat subjects, a more meaningful comparison of the statistical properties of scatterers in healthy and diseased tissues can be made.

ACKNOWLEDGMENTS

Thanks to James P. Blue and Rita J. Miller, DVM, for their technical assistance. This work was supported by NIH Grant Nos. CA09067 and CA79179.

- ¹J. F. Greenleaf and C. M. Sehgal, *Biologic System Evaluation with Ultrasound* (Springer, New York, 1992), pp. 101–103.
- ²M. F. Insana, "Modeling acoustic backscatter from kidney microstructure using an anisotropic correlation function," *J. Acoust. Soc. Am.* **97**, 649–655 (1995).
- ³Y. Miyazaki, "Light scattering of laser beams by random microinhomogeneities in glasses and polymers," *Jpn. J. Appl. Phys.* **13**, 1238–1248 (1974).
- ⁴M. Tobiyama, I. Endo, T. Monaka, Y. Sumi, H. Uchida, N. Yamamoto, K. Yoshida, K. Watanabe, T. Ohba, K. Baba, and T. Emura, "Determination of atomic form factors by means of coherent bremsstrahlung," *Phys. Rev. B* **44**, 9248–9258 (1991).
- ⁵D. K. Wilson, J. G. Brasseur, and K. E. Gilbert, "Acoustic scattering and the spectrum of atmospheric turbulence," *J. Acoust. Soc. Am.* **105**, 30–34 (1999).
- ⁶E. J. Feleppa, F. L. Lizzi, D. J. Coleman, and M. M. Yaremko, "Diagnostic spectrum analysis in ophthalmology: A physical perspective," *Ultrasound Med. Biol.* **12**, 623–631 (1986).
- ⁷F. L. Lizzi, M. Ostromogilsky, E. J. Feleppa, M. C. Rorke, and M. M. Yaremko, "Relationship of ultrasonic spectral parameters to features of tissue microstructure," *IEEE Trans. Ultrason. Ferroelectr. Freq. Control* **33**, 319–329 (1986).
- ⁸M. F. Insana, T. J. Hall, and J. L. Fishback, "Identifying acoustic scattering sources in normal renal parenchyma from the anisotropy in acoustic properties," *Ultrasound Med. Biol.* **17**, 613–626 (1991).
- ⁹K. K. Shung and G. A. Thieme, *Ultrasonic Scattering in Biological Tissues* (CRC Press, Boca Raton, 1993).
- ¹⁰J. A. Faran, Jr., "Sound scattering by solid cylinders and spheres," *J. Acoust. Soc. Am.* **23**, 405–418 (1951).
- ¹¹R. H. Silverman, M. J. Rondeau, F. L. Lizzi, and D. J. Coleman, "Three-

- dimensional high-frequency ultrasonic parameter imaging of anterior segment pathology," *Ophthalmology* **102**, 837–843 (1995).
- ¹²P. M. Morse and K. U. Ingard, *Theoretical Acoustics* (McGraw-Hill, New York, 1968).
- ¹³F. L. Lizzi, M. Greenbaum, E. J. Feleppa, and M. Elbaum, "Theoretical framework for spectrum analysis in ultrasonic characterization," *J. Acoust. Soc. Am.* **73**, 1366–1373 (1983).
- ¹⁴M. F. Insana, R. F. Wagner, D. G. Brown, and T. J. Hall, "Describing small-scale structure in random media using pulse-echo ultrasound," *J. Acoust. Soc. Am.* **87**, 179–192 (1990).
- ¹⁵M. F. Insana and T. J. Hall, "Parametric ultrasound imaging from backscatter coefficient measurements: Image formation and interpretation," *Ultrasound Imaging* **12**, 245–267 (1990).
- ¹⁶F. L. Lizzi, M. Astor, T. Liu, C. Deng, D. J. Coleman, and R. H. Silverman, "Ultrasonic spectrum analysis for tissue assays and therapy evaluation," *Int. J. Imaging Syst. Technol.* **8**, 3–10 (1997).
- ¹⁷D. Nicholas, "Evaluation of backscattering coefficients for excised human tissues: Results, interpretation, and associated measurements," *Ultrasound Med. Biol.* **8**, 17–28 (1982).
- ¹⁸D. K. Nassiri and C. R. Hill, "The use of angular scattering measurements to estimate structural parameters of human and animal tissues," *J. Acoust. Soc. Am.* **79**, 2048–2054 (1986).
- ¹⁹K. A. Topp, J. F. Zachary, and W. D. O'Brien, Jr., "Quantifying B-mode images of *in vivo* rat mammary tumor with frequency dependence of backscatter," *J. Ultrasound Med.* **20**, 605–612 (2001).
- ²⁰M. Akita and M. Ueda, "The effect of windowing on spectral estimation of echoes scattered by a random medium," *J. Acoust. Soc. Am.* **83**, 1243–1248 (1988).
- ²¹M. F. Insana, E. L. Madsen, T. J. Hall, and J. A. Zagzebski, "Tests of the accuracy of a data reduction method for determination of acoustic backscatter coefficients," *J. Acoust. Soc. Am.* **79**, 1230–1236 (1986).
- ²²J. F. Chen, J. A. Zagzebski, and E. L. Madsen, "Tests of backscatter coefficient measurement using broadband pulses," *IEEE Trans. Ultrason. Ferroelectr. Freq. Control* **40**, 603–607 (1993).
- ²³K. A. Wear, R. F. Wagner, M. F. Insana, and T. J. Hall, "Application of autoregressive spectral analysis to cepstral estimation of mean scatterer spacing," *IEEE Trans. Ultrason. Ferroelectr. Freq. Control* **40**, 50–58 (1993).
- ²⁴G. A. Teotica, R. J. Miller, L. A. Frizzell, J. F. Zachary, and W. D. O'Brien, Jr., "Attenuation coefficient estimates of mouse and rat chest wall," *IEEE Trans. Ultrason. Ferroelectr. Freq. Control* **48**, 593–600 (2001).
- ²⁵R. A. Sigelmann and J. M. Reid, "Analysis and measurement of ultrasound backscattering from an ensemble of scatterers excited by sine-wave bursts," *J. Acoust. Soc. Am.* **53**, 1351–1355 (1973).
- ²⁶M. O'Donnell and J. G. Miller, "Quantitative broadband ultrasonic backscatter: An approach to nondestructive evaluation in acoustically inhomogeneous materials," *J. Appl. Phys.* **52**, 1056–1065 (1981).
- ²⁷M. L. Oelze and W. D. O'Brien, Jr., "Comparisons of frequency-dependent attenuation-compensation functions for ultrasonic signals backscattered from random media," *J. Acoust. Soc. Am.* **111**, 2308–2319 (2002).
- ²⁸S. L. Bridal, P. Fornes, P. Bruneval, and G. Berger, "Parametric (integrated backscatter and attenuation) images constructed using backscattered radio frequency signals (25–56 MHz) from human aortae *in vitro*," *Ultrasound Med. Biol.* **23**, 215–229 (1997).
- ²⁹J. A. Zagzebski, Z. F. Lu, and L. X. Yao, "Quantitative ultrasound imaging: *in vitro* results in normal liver," *Ultrasound Imaging* **15**, 335–351 (1983).
- ³⁰E. J. Feleppa, T. Liu, A. Kalisz, M. C. Shao, N. Fleshner, and V. Reuter, "Ultrasonic spectral-parameter imaging of the prostate," *Int. J. Imaging Syst. Technol.* **8**, 11–25 (1997).
- ³¹M. F. Insana, T. J. Hall, J. G. Wood and Z-Y Yan, "Renal ultrasound using parametric imaging techniques to detect changes in microstructure and function," *Invest. Radiol.* **28**, 720–725 (1993).
- ³²F. L. Lizzi, M. Astor, A. Kalisz, T. Liu, D. J. Coleman, R. Silverman, R. Ursea, and M. Rondeau, "Ultrasonic spectrum analysis for assays of different scatterer morphologies: Theory and very-high frequency clinical results," *Proceedings of the 1996 IEEE Ultrasonic Symposium*, 1155–1159 (1996).
- ³³P. Chaturvedi and M. F. Insana, "Error bounds on ultrasonic scatterer size estimates," *J. Acoust. Soc. Am.* **100**, 392–399 (1996).